Short Note

(E)-2-(6-(4′-(Diphenylamino)-[1,1′-biphenyl]-2-yl)-[1,2,5]oxadiazolo[3,4-*b*]pyrazin-5(4*H*)-ylidene)-2-(6-(4′-(diphenylamino)-[1,1′-biphenyl]-2-yl)-[1,2,5]oxadiazolo[3,4-*b*]pyrazin-5-yl)acetonitrile

Yuriy A. Kvashnin [1,2], Pavel A. Slepukhin [1,2], Denis A. Gazizov [1], Ekaterina F. Zhilina [1], Gennady L. Rusinov [1,2], Egor V. Verbitskiy [1,2,*] and Valery N. Charushin [1,2]

1   I. Postovsky Institute of Organic Synthesis, Ural Branch of the Russian Academy of Sciences, S. Kovalevskaya Str. 22, Ekaterinburg 620108, Russia
2   Chemical Engineering Institute, Ural Federal University, Mira Str. 19, Ekaterinburg 620002, Russia
*   Correspondence: verbitskye@yandex.ru

Abstract: [1,2,5]Oxadiazolo[3,4-*b*]pyrazines are of great interest due to their promising photophysical and electrochemical properties, as well their potential use in a wide range of electronic devices. Herein, we report on the preparation of the unexpected product derived from the interaction of 2′-([1,2,5]oxadiazolo[3,4-*b*]pyrazin-5-yl)-*N,N*-diphenyl-[1,1′-biphenyl]-4-amine with 2-cyanoacetic acid under basic conditions. The resulting product was characterized using ^{1}H and ^{13}C NMR spectra, high resolution mass spectrometry, Fourier-transform infrared spectroscopy (FTIR), and X-ray diffraction analyses. Furthermore, its photophysical and electrochemical properties were studied using cyclic voltammetry, UV–Vis, and emission spectroscopy. The experimental results have been further rationalized through theoretical DFT calculations.

Keywords: 1,2,5-oxadiazolo[3,4-*b*]pyrazines; 2-cyanoacetic acid; organic semiconductors

1. Introduction

[1,2,5]Oxadiazolo[3,4-*b*]pyrazines, also known as furazanopyrazines, have gained considerable attention from researchers working in the fields of both medicinal chemistry [1] and material science as promising high-energy compounds [2], molecular magnets [3], and nonlinear optical [4], sensor [5], and semiconductor materials [6,7]. One of the modern methods for modifying the furazanopyrazine core is the direct functionalization of the C–H bond through the metal-free nucleophilic aromatic substitution of hydrogen (the so-called S_N^H reactions) [8].

Previously, it has been shown that 1,4-diazine derivatives react with CH-active methylene compounds to form either furo[2,3-*b*]prazines (route I) or to give the corresponding ylidene derivatives (route II) (Scheme 1).
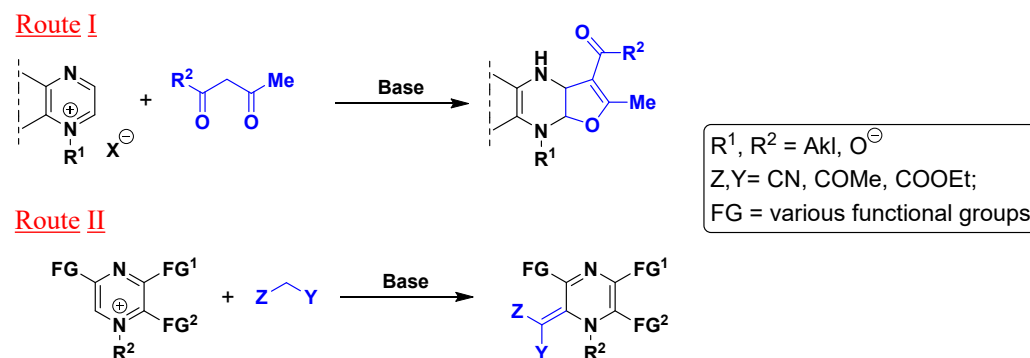

Scheme 1. Two alternative routes for the reactions of 1,4-diazines with CH-active methylene compounds.

Herein, we report on the synthesis, structural characterization, optical, and electrochemical properties of the product deriving from the double nucleophilic attack of 2-cyanoacetic acid at the C-6 position of 5-aryl-substituted furazano[3,4-*b*]pyrazine.

2. Results and Discussion

2.1. Synthesis of (E)-2-(6-(4′-(Diphenylamino)-[1,1′-biphenyl]-2-yl)-[1,2,5]oxadiazolo[3,4-b]pyrazin-5(4H)-ylidene)-2-(6-(4′-(diphenylamino)-[1,1′-biphenyl]-2-yl)-[1,2,5]oxadiazolo[3,4-b]pyrazin-5-yl)acetonitrile (3)

The formation of (*E*)-2-(6-(4′-(diphenylamino)-[1,1′-biphenyl]-2-yl)-[1,2,5]oxadiazolo [3,4-*b*]pyrazin-5(4*H*)-ylidene)-2-(6-(4′-(diphenylamino)-[1,1′-biphenyl]-2-yl)-[1,2,5]oxadiazolo [3,4-*b*]pyrazin-5-yl)acetonitrile (**3**) was first demonstrated as a result of a double attack of 2-cyanoacetic acid (**2**) at the C(6) position of 5-aryl substituted [1,2,5]oxadiazolo[3,4-*b*]pyrazine (**1**) followed by the decarboxylation reaction. The reaction was found to proceed smoothly in acetonitrile at 50 °C for 4 h in the presence of diazabicyclo[2.2.2]octane (DABCO) as the base (Scheme 2). Then, the reaction mixture was allowed to stand overnight at room temperature (TLC control), and product **3** was isolated at a moderate yield (57%). It is worth noting that all attempts to carry out the reaction with 5-phenyl-, 5-(thiophen-2-yl)- or 5-(thiophen-3-yl)-furazanopyrazine have failed due to the formation of rather complicated multicomponent mixtures.
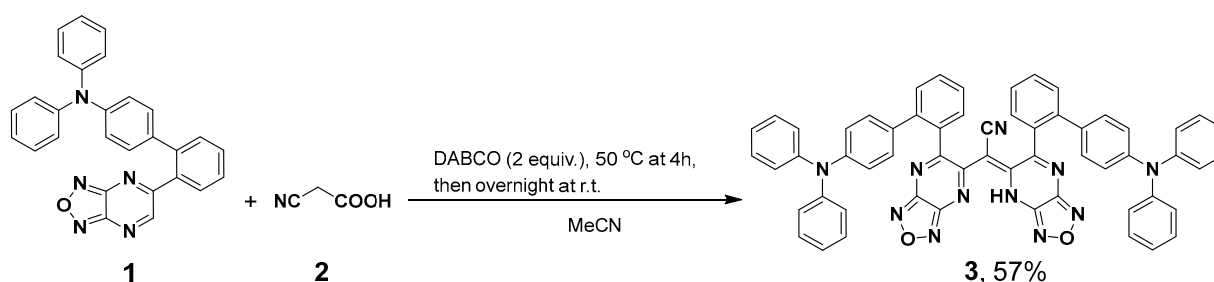
Scheme 2. Synthesis of compound **3**.

2.2. Crystal Structure of Compound (3)

The molecular structure of **3** in the solid state was ascertained using X-ray diffraction analyses on suitable single crystals, which were grown from acetonitrile solution via the slow evaporation of the solvent at room temperature. Figure 1 shows a representation of a single molecule of compound **3**. The structure was crystallized in the centrosymmetric space group. The molecule has a two-turn spiral conformation (Figure 1). One pyrazine moiety had a 1,2-dihydro-stucture and formed an intramolecular H-bond N…HN with the second pyrazine ring. The CN group is included in the system of the conjugated π-bonds and is placed in the trans-position towards the ring nitrogen. Triphenylamine groups have a propeller-like conformation with the planar geometry of their *N*-atoms. No specific intermolecular contacts in the crystal have been observed.

2.3. Photophysical and Electrochemical Properties of the Compound (3)

The structure of the obtained compound **3** was also proved using Fourier transform infrared spectroscopy (FTIR) (Figure S3). The –C≡N stretch band occurred at 2207 cm^{-1}. The very weak NH stretch IR band was observed at 3292 cm^{-1}, and the deformation band was seen at 1633 cm^{-1}. The CH stretching vibrations of phenyls gave rise to IR bands in the 3020–3060 cm^{-1} region. The group of intense bands in the 1610–1430 cm^{-1} region could be attributed to ring CC, CN bonds vibrations.
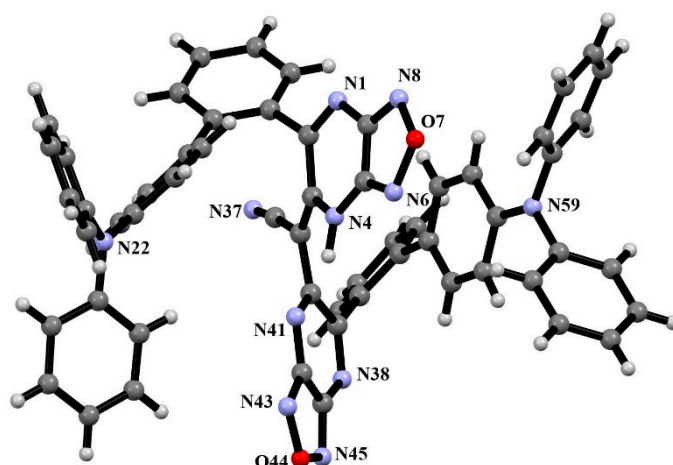
Figure 1. Ball and sticks model of the compound according to XRD data.

The absorption, excitation, and emission spectra of compound **3** were recorded in CH$_2$Cl$_2$ (Figures 2 and 3, Table 1). Three main absorption bands can be distinguished in the absorption spectrum. The first one, with a maximum at 307 nm (ε = 43,200 M^{-1}cm^{-1}), can be attributed to allowed π-π* transitions in donor fragments of the molecule. The second band, at 468 nm, can be tentatively attributed to an initially relaxed locally excited (LE) state, while the longest wavelength band probably corresponds to the more twisted state with pronounced intramolecular charge transfer (CT) via a conical intersection [9,10]. Emission has not been observed upon excitation in the range of the long-wavelength absorption band. Figure 3 shows the steady-state fluorescence spectra of **3** in CH$_2$Cl$_2$ solution. Compound **3** exhibited weak green fluorescence, probably from the LE state, with an absolute fluorescence quantum yield of less than 0.01.
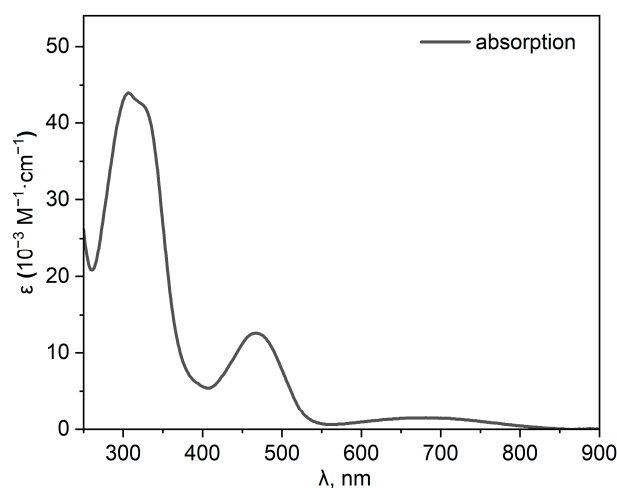
Figure 2. Absorption spectrum of **3** in CH$_2$Cl$_2$.

A cyclic voltammogram of the new compound **3** was obtained on a platinum electrode in a CH$_2$Cl$_2$ solution containing tetrabutylammonium tetrafluoroborate as a supporting electrolyte (see Figure 4, Table 2). The first electroreduction peak of compound **3** was quasi-reversible at a potential superposition rate of 0.1 V·s^{-1}, and electrooxidation at the same time was irreversible.

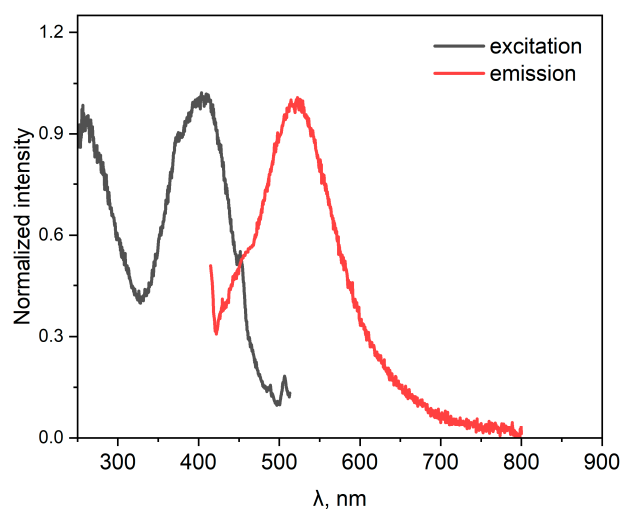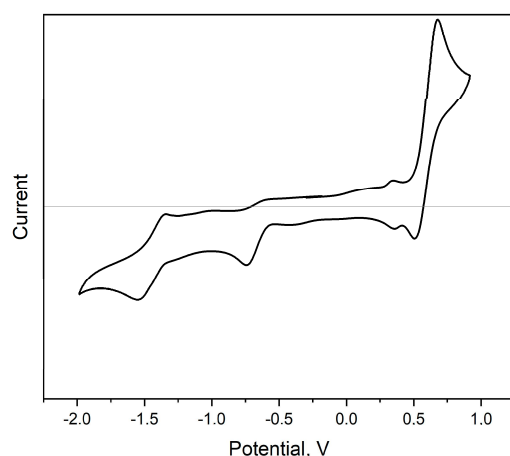**Figure 3.** Excitation (*black*) and emission (*red*) spectra of **3** in CH_2Cl_2.

Figure 4. Cyclic voltammogram curve (vs. Fc/Fc$^+$) for compound **3** in CH_2Cl_2 solution.

Table 1. Optical properties of compound **3**.

Compound	UV–Vis Absorption		Fluorescence		Φ, %
	$\lambda_{abs}{}^{max}$, nm	ε_{max}, M^{-1} cm^{-1}	Excitation λ_{ex}, nm	Emission λ_{em}, nm	
3	307	43,200	260, 405	523	<1
	468	12,500			
	680	1500			

Φ—the absolute quantum yield.

The energies of frontier molecular orbitals (E_{HOMO} and E_{LUMO}) and the energy gap (E_g) are important criteria affecting the electronic and conductive properties of materials. There is evidence of a direct correlation between the types of charge carriers in organic thin-film transistors (OTFTs) and the experimentally estimated levels of frontier molecular orbitals. It has been shown that materials with LUMO < −3.15 eV and HOMO < −5.60 eV demonstrate strictly *n*-type semiconductor behavior, which is explained by high barriers for hole injection [11]. Thus, we decided to compare the HOMO and LUMO energies, as well as the band gap, obtained from optical and electrochemical data (Table 2). Additionally, we carried out quantum-chemical calculations of the theoretical band gap. In calculations based on electrochemical data, half-wave potentials were used instead of onset potentials, since they are more reliable in the case of the cyclic voltammetry of single molecule solution [12].

Table 2. Electrochemical properties and energies of frontier molecular orbitals and the band gap of compound **3**.

E^h_{red} [a], eV	E^h_{ox} [a], eV	E^{el}_{LUMO}, eV	E^{el}_{HOMO}, eV	E^{DFT}_{LUMO}, [a] eV	E^{DFT}_{HOMO}, [a] eV	E_g^{opt}, [b] eV	E_g^{el}, eV	E_g^{DFT}, eV
−0.63	0.58	−4.17	−5.38	−3.65	−5.28	1.46	1.21	1.63

E^h—the half-wave potential. [a] Calculated at B3LYP/6-311G(d,p) level of theory. [b] $E_g^{opt} = hc/\lambda = 1240/\lambda_{onset}$; λ_{onset}—wavelength of the onset (edge) of the lowest-energy absorbance band.

Based on the data obtained, the synthesized polycyclic systems can be attributed to narrow-gap ($E_g \sim 1.2–1.6$ eV) *n*-type organic semiconductors, the energies of the frontier molecular orbitals of which are comparable with many known *n*-type semiconductors [13].

3. Materials and Methods

All chemicals were purchased from Sigma-Aldrich and used without further purification. The ^{1}H and ^{13}C NMR spectra were recorded on a Bruker AVANCE-500 instruments using Me_4Si as an internal standard. Elemental analysis was carried out on a Eurovector EA 3000 automated analyzer. High-resolution mass spectrometry was performed using a Bruker maXis Impact HD spectrometer. Melting points were determined on Boetius combined heating stages and were not corrected.

Column chromatography was carried out using Alfa Aesar silica gel 0.040–0.063 mm (230–400 mesh). The progress of reactions and the purity of compounds were checked with TLC on Sorbfil plates (Russia), in which the spots were visualized with UV light (λ 254 or 365 nm).

The IR spectrum was recorded on a PerkinElmer Spectrum Two FT-IR spectrometer (Perkin-Elmer, Waltham, MA, USA) using the total internal reflection accessory with a diamond crystal in the $4000 - 400$ cm^{-1}.

UV–Vis spectra were recorded for $10^{-5} - 10^{-6}$ M CH_2Cl_2 solutions with a Shimadzu UV-2600 spectrophotometer. Fluorescence spectra were recorded on the FS5 spectrofluorometer (Kirkton Campus, Livingston, Edinburgh Instruments, Livingston, UK) using standard 1 cm quartz cells at room temperature. The absolute quantum yield was measured on the FS5 spectrofluorometer using the SC-30 integrating sphere at $\lambda_{Ex} = 350$ nm.

Cyclic voltammetry was carried out on a Metrohm Autolab PGSTAT128N potentiostat with a standard three-electrode configuration. Typically, a three-electrodes cell equipped with a glass carbon working electrode, a Ag/AgNO$_3$ (0.01 M) reference electrode, and a glass carbon rod counter electrode were employed. The measurements were performed in CH2Cl2 with tetrabutylammonium hexafluorophosphate (0.1 M) as the supporting electrolyte under an argon atmosphere at a scan rate of 100 mV/s. The potential of the reference electrode was calibrated by using the ferrocene/ferrocenium redox couple (Fc/Fc$^+$).

The HOMO and LUMO energy values were estimated from the half-wave potentials of the first independent oxidation and reduction process, respectively, according to the following equations:

$$E_{HOMO} \text{ (eV)} = -[E^h_{ox} - E_{1/2}(Fc/Fc^+) + 4.8] \tag{1}$$

$$E_{LUMO} \text{ (eV)} = -[E^h_{red} - E_{1/2}(Fc/Fc^+) + 4.8] \tag{2}$$

DFT calculations were performed using the Orca 5.0.3 program. The ground-state geometry optimizations were performed at the B3LYP/6-311G(d,p) level of theory in the gas phase. Frequency analyses were carried out at the same theoretical level to ensure that the optimized geometries corresponded to a local minimum on the potential energy surface; all compounds were characterized by only real vibrational frequencies.

The XRD analysis of the single crystal of **3** was carried out using an "Xcalibur 3" diffractometer on standard procedure (Mo*K*-irradiation, graphite monochromator, ω-scans

with 1° step, T = 295(2) K). Empirical absorption correction was applied. The solution and refinement of the structures were accomplished using Olex2 program package [14]. The structure was solved by the method of the intrinsic phases in the ShelXT program and was refined by ShelXL by the full-matrix least-squared method for non-hydrogen atoms [15]. The H-atoms at C–H bonds were placed in the calculated positions; the H-atom at N–H bond was refined independently in isotropic approximation.

Crystal data for $C_{58}H_{37}N_{11}O_2$ (M = 919.98 g/mol): monoclinic, space group P2$_1$/c, a = 17.3019(12) Å, b = 10.5780(5) Å, c = 26.011(2) Å, β = 107.778(8)°, V = 4533.2(6) Å^3, Z = 4, T = 295(2) K, μ(Mo K$_\alpha$) = 0.086 mm^{-1}, D_{calc} = 1.348 g/cm^3, 35,921 reflections measured (7.14° ≤ 2Θ ≤ 56.564°), 10,615 unique (R_{int} = 0.0643, R_{sigma} = 0.0716), which were used in all calculations. The final R_1 = 0.0664, wR_2 = 0.1665 (I > 2σ(I)) and R_1 = 0.1329, wR_2 = 0.2263 (all data), and GooF = 1.026. Largest diff. peak/hole 0.21/–0.20 ēÅ^{-3}. The structure was registered in the Cambridge Structural Database with the number CCDC 2270993. These data can be obtained free of charge via www.ccdc.cam.ac.uk (accessed on 16 August 2023).

*Synthesis of (E)-2-(6-(4′-(Diphenylamino)-[1,1′-biphenyl]-2-yl)-[1,2,5]oxadiazolo[3,4-b]pyrazin-5(4H)-ylidene)-2-(6-(4′-(diphenylamino)-[1,1′-biphenyl]-2-yl)-[1,2,5]oxadiazolo[3,4-b]pyrazin-5-yl)acetonitrile (**3**) (Supplementary Materials)*

A mixture of 2′-([1,2,5]oxadiazolo[3,4-*b*]pyrazin-5-yl)-*N*,*N*-diphenyl-[1,1′-biphenyl]-4-amine **1** (110 mg, 0.25 mmol), 2-cyanoacetic acid **2** (22 mg, 0.25 mmol), and 1,4-diazabicyclo octane (DABCO) (56 mg, 0.5 mmol) was dissolved in acetonitrile (15 mL). The mixture was stirred for 4 h at 50 °C and then cooled to room temperature overnight. After that, conc. HCl (0.1 mL) was added and the solvent was evaporated under reduced pressure. The residue was separated using silica gel column chromatography (eluent—CH_2Cl_2). The yield was 65 mg (57%), as a dark brown solid. Mp = 289–292 °C. R_f = 0.3 (CH_2Cl_2). IR spectrum, ν, cm^{-1}: 3292 (ν$_{NH}$), 3059, 3029 (ν$_{CH\ arom.}$), 2207 (ν$_{CN}$), 1633 (δ$_{NH}$), 1589, 1512, 1491, 1471, 1440, 1333, 1301, 1275, 1205, 1193, 1110, 1023, 1004, 772, 751, 733, 704, 696. ^{1}H NMR (500 MHz, CDCl$_3$) δ 11.85 (s, 1H), 7.67 (dd, *J* = 7.7, 1.3 Hz, 2H), 7.56 (td, *J* = 7.6, 1.4 Hz, 2H), 7.47 (td, *J* = 7.6, 1.2 Hz, 2H), 7.30–7.26 (m, 7H), 7.25 (s, 3H), 7.13–7.07 (m, 4H), 7.05–7.01 (m, 8H), 6.72–6.68 (m, 4H), 6.65–6.56 (m, 4H). ^{13}C NMR (126 MHz, CDCl$_3$) δ 166.00, 150.60, 150.51, 148.09, 146.40, 144.97, 141.33, 134.88, 132.49, 131.22, 130.19, 129.83, 129.72, 129.53, 129.47, 128.20, 125.89, 125.44, 124.39, 124.04, 120.63, 119.95, 110.61, 90.49. HRMS (APCI), *m*/*z*: calcd. for $C_{58}H_{38}N_{11}O_2$ [M + H]$^+$ 920.3204 and found 920.3205. Anal. calcd. for $C_{58}H_{37}N_{11}O_2$ (920,0090): C, 75.72; H, 4.05; N, 16.75. Found: C, 75.62; H, 3.99; N, 16.92.

Supplementary Materials: The following are available online, Figure S1. ^{1}H NMR spectrum of **3**; Figure S2. ^{13}C NMR (151 MHz, CDCl$_3$) spectrum of **3**; Figure S3. IR spectrum of **3**; Figure S4. HRMS data of **3**; Cartesian coordinates for the optimized geometry of compound **3**; Figure S5. HOMO and LUMO of compound **3**; Figure S6. Superposition of the molecular structure of compound **3** in the single crystal (purple) and the optimal geometry for compound **3** in the gas phase according to DFT calculations (RMSD = 1.6 Å).

Institutional Review Board Statement: Not applicable.

Informed Consent Statement: Not applicable.

Data Availability Statement: Not applicable.

References

1. Mancini, R.S.; Barden, C.J.; Weaver, D.F.; Reed, M.A. Furazans in Medicinal Chemistry. *J. Med. Chem.* **2021**, *64*, 1786–1815. [CrossRef] [PubMed]
2. Fershtat, L.L. Recent advances in the synthesis and performance of 1,2,4,5-tetrazine-based energetic materials. *FirePhysChem* **2023**, *3*, 78–87. [CrossRef]
3. Ovcharenko, V.I.; Sheremetev, A.B.; Strizhenko, K.V.; Fokin, S.V.; Romanenko, G.V.; Bogomyakov, A.S.; Morozov, V.A.; Syroeshkin, M.A.; Kozmenkova, A.Y.; Lalov, A.V.; et al. Novel organic magnet derived from pyrazine-fused furazans. *Mendeleev Commun.* **2021**, *31*, 784–788. [CrossRef]
4. Verbitskiy, E.V.; Achelle, S.; Bureš, F.; le Poul, P.; Barsella, A.; Kvashnin, Y.A.; Rusinov, G.L.; Guen, F.R.-L.; Chupakhin, O.N.; Charushin, V.N. Synthesis, photophysical and nonlinear optical properties of [1,2,5]oxadiazolo[3,4-*b*]pyrazine-based linear push-pull systems. *J. Photochem. Photobiol. A* **2021**, *404*, 112900. [CrossRef]
5. Verbitskiy, E.V.; Kvashnin, Y.A.; Baranova, A.A.; Khokhlov, K.O.; Chuvashov, R.D.; Yakovleva, Y.A.; Makarova, N.I.; Vetrova, E.V.; Metelitsa, A.V.; Rusinov, G.L.; et al. Novel fluorophores based on imidazopyrazine derivatives: Synthesis and photophysical characterization focusing on solvatochromism and sensitivity towards nitroaromatic compounds. *Dye. Pigment.* **2019**, *168*, 248–256. [CrossRef]
6. Kvashnin, Y.A.; Verbitskiy, E.V.; Eltsov, O.S.; Slepukhin, P.A.; Tameev, A.R.; Nekrasova, N.V.; Rusinov, G.L.; Nunzi, J.-M.; Chupakhin, O.N.; Charushin, V.N. Dibenzo[*f,h*]furazano[3,4-*b*]quinoxalines: Synthesis by intramolecular cyclization through direct transition metal-free C–H functionalization and electrochemical, photophysical, and charge mobility characterization. *ACS Omega* **2020**, *5*, 8200–8210. [CrossRef] [PubMed]
7. Steparuk, A.S.; Kvashnin, Y.A.; Rusinov, G.L.; Verbitskiy, E.V.; Aleksandrov, A.E.; Lypenko, D.A.; Tameev, A.R.; Charushin, V.N. The first application of push-pull systems based on 1,2,5-oxadiazolo[3,4-*b*]pyrazine in organic light-emitting diodes and perovskite solar cells. *Russ. Chem. Bull.* **2023**, *72*, 527–533. [CrossRef]
8. Kvashnin, Y.A.; Verbitskiy, E.V.; Rusinov, G.L.; Charushin, V.N. Modification and application of 1,2,5-oxadiazolo[3,4-*b*]pyrazine derivatives: Highlights and perspectives. *Russ. Chem. Bull.* **2022**, *71*, 1342–1362. [CrossRef]
9. Grabowski, Z.R.; Rotkiewicz, K.; Siemiarczuk, A. Dual fluorescence of donor-acceptor molecules and the Twisted Intramolecular Charge Transfer (TICT) states. *J. Lumin.* **1979**, *18–19*, 420–424. [CrossRef]
10. Grabowski, Z.R.; Rotkiewicz, K.; Rettig, W. Structural Changes Accompanying Intramolecular Electron Transfer: Focus on Twisted Intramolecular Charge-Transfer States and Structures. *Chem. Rev.* **2003**, *103*, 3899–4032. [CrossRef] [PubMed]
11. Purushotham, U.; Narahari Sastry, G. Conjugate acene fused buckybowls: Evaluating their suitability for *p*-type, ambipolar and *n*-type air stable organic semiconductors. *Phys. Chem. Chem. Phys.* **2013**, *15*, 5039–5048. [CrossRef] [PubMed]
12. Eakins, G.L.; Cooper, M.W.; Gerasimchuk, N.N.; Phillips, T.J.; Breyfogle, B.E.; Stearman, C.J. Structural influences impacting the role of the 9-ylidene bond in the electronic tuning of structures built upon 9-fluorenylidene scaffolds. *Can. J. Chem.* **2013**, *91*, 1059–1071. [CrossRef]
13. Gao, X.; Hu, Y. Development of *n*-type organic semiconductors for thin film transistors: A viewpoint of molecular design. *J. Mater. Chem. C* **2014**, *2*, 3099–3117. [CrossRef]
14. Dolomanov, O.V.; Bourhis, L.J.; Gildea, R.J.; Howard, J.A.K.; Puschmann, H. OLEX2: A complete structure solution, refinement and analysis program. *J. Appl. Cryst.* **2009**, *42*, 339–341. [CrossRef]
15. Sheldrick, G.M. SHELXT—Integrated space-group and crystal-structure determination. *Acta Cryst.* **2015**, *A71*, 3–8. [CrossRef] [PubMed]